Composites: Part A 184 (2024) 108275

Contents lists available at ScienceDirect

Composites Part A

journal homepage: www.elsevier.com/locate/compositesa

On how pseudo-ductility modifies the translaminar fracture toughness of composites and the nominal strength of centre-cracked specimens

A. Subramani, P. Maimí *, J. Costa

AMADE, Escola Politecnica Superior, Universitat de Girona, Girona, 17071, Spain

ARTICLE INFO

Keywords:
Pseudo-ductility
Translaminar toughness
Nominal strength
Finite element analysis

ABSTRACT

Among the efforts to revert the traditionally brittle characteristic of laminated composites, pseudo-ductility relies on utilising hybridisation to stimulate sub-critical damage mechanisms. However, how such pseudo-ductility would translate into an increase in material toughness or an improvement in the strength of the sub-components remains unclear. To elucidate this, we perform a numerical study departing from a parameterised pseudo-ductile model implemented in a finite element model. We use non-dimensional analysis to investigate the effect of the two most relevant parameters: pseudo-ductile strain (ε_d) and the ratio of ultimate strength to pseudo-ductile yield strength (σ_f/σ_y). We infer material toughness from the simulation of Compact Tension specimens, and it is shown to increase linearly with ε_d, and non-linearly with σ_f/σ_y but tends to a plateau. Then, the simulation of Centre Cracked scaled specimens reveal that the nominal strength increases on the elastic limit extreme (large specimens) but decreases below a given size.

1. Introduction

The attainment of a ductility alike behaviour in the stress–strain response, pseudo-ductility, is an active area of research in laminated composite materials to mitigate their inherent brittleness [1–7]. Endeavours are based on promoting controlled sub-critical damage mechanisms like ply fragmentation and dispersed delamination [1–6], ply re-orientation [8] or tortuous crack paths [9]. The aim is to increase the residual load carrying capacity past the damage initiation, which may also increase the fracture toughness eventually [10]. However, the soundness of this prospect is arguable as it is unclear how pseudo-ductility translates into an enhanced resistance to crack propagation (translaminar fracture toughness). Likewise, it is unclear how pseudo-ductility can modify the size-effect of notched structures, which is characteristic of quasi-brittle structures like composites and concrete (i.e., the nominal strength decreases when the structure is scaled up while the geometric ratios and the material properties are kept constant) [11]. Previous investigations on pseudo-ductile laminates investigated only the un-notched tensile strength and the nominal strength of open-hole and centre-cracked specimens with a single crack length [5]. Translaminar toughness, among others, is a crucial property influencing nominal strength. Thus, the effect of pseudo-ductility on toughness and size-effect deserves further research in unison.

Ply-blocking of Low Strain (LS) and High Strain (HS) plies to form sub-laminates (e.g., glass–carbon–glass in the same orientation, see Fig. 1b) is the typical way to achieve pseudo-ductility [1,3,4,7]. The first damage mechanism, fragmentation, is the intra or translaminar breaking of LS plies. Fragmentation is followed by the delamination at the LS/HS, and HS/LS ply interfaces, starting from both sides of the fragment end as a result of the increased peel stresses. With the increasing strain, the density of the fragmentation and the dispersed delamination reaches saturation. Upon saturation, the load is carried mostly by the HS plies in the laminate, eventually leading to the laminate failure (b–c in Fig. 1a). The stress–strain response of such an idealised pseudo-ductile uni-directional laminate is presented in Fig. 1a (solid line) [1–3,12,13]. This sequence of failure mechanism depends on several factors like the proportion of LS to HS material, the absolute thickness of the LS and HS plies, stiffness variation between LS and HS material and interlaminar toughness [1–3,12,13].

In this work, the term "yield stress" (σ_y) is not used in the traditional sense, it represents the knee-point in the stress–strain curve upon which it deviates from the initial modulus. The degree of pseudo-ductility in a laminate is characterised by the pseudo-ductile strain (ε_d): the difference in strain between the failure strain (ε_f) and the strain based on the initial modulus at the failure stress (σ_f), see Fig. 1a.

Generally, quasi-isotropic pseudo-ductile laminates are formed by stacking the uni-directional pseudo-ductile sub-laminates in the desired orientation, see Fig. 1b. For a quasi-isotropic pseudo-ductile laminate, the idealised pseudo-ductile behaviour (Fig. 1a, dotted line) is further simplified by considering that the plateau region post-yielding

* Corresponding author.
E-mail address: pere.maimi@udg.edu (P. Maimí).

https://doi.org/10.1016/j.compositesa.2024.108275
Received 16 September 2023; Received in revised form 28 April 2024; Accepted 19 May 2024
Available online 25 May 2024

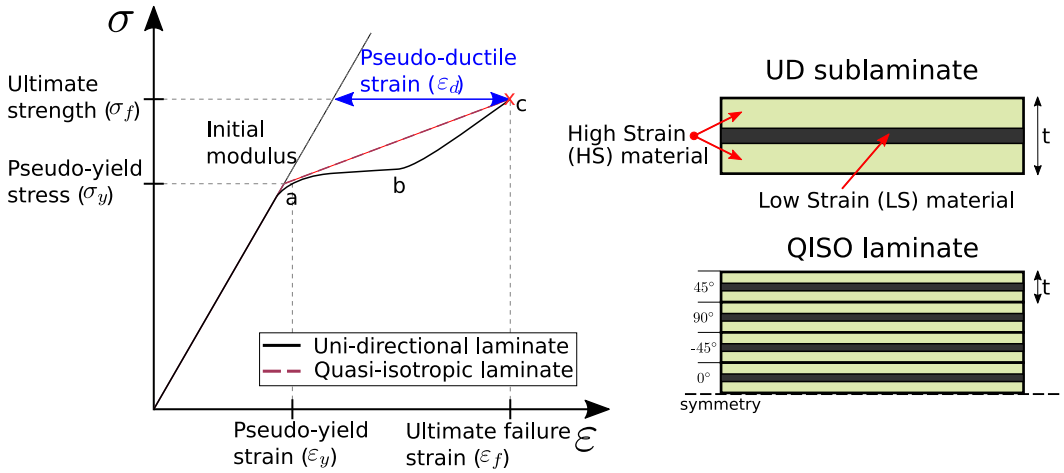

Fig. 1. Pseudo-ductile material behaviour (a) Idealised pseudo-ductile behaviour of uni-directional and quasi-isotropic hybrid laminates under tensile loading. (b) Examples of typical ply-by-ply pseudo-ductile laminates.

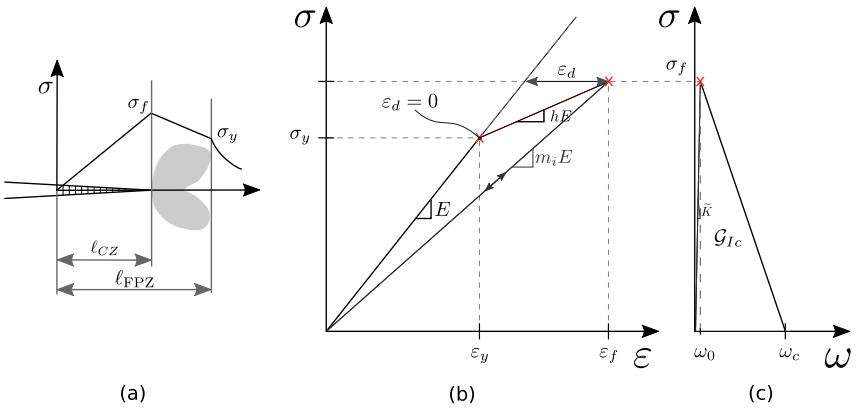

Fig. 2. Description of a fracture process zone and the constitutive pseudo-ductile material behaviour. (b) Linear elastic pseudo-ductile region to represent intrinsic behaviour and (c) Traction-separation behaviour (Cohesive law) to represent the extrinsic behaviour. The modulus ratio, $h \in [0, 1]$.

is negligible. This is because the fragmentation at all the LS plies may not necessarily start at once and is constrained by the surrounding sub-laminates. This is consistent with the experimentally observed pseudo-ductile quasi-isotropic laminate behaviour [4–7]. Quasi-isotropic pseudo-ductile behaviour with considerable plateau prior to the 'hardening' has also been demonstrated [14]. However, these laminates generally show unacceptable vertical load drop following fragmentation. Hence, we focus only on the pseudo-ductile response of the successful quasi-isotropic laminates due to their application potential.

The resistance to crack propagation in a material depends on the damage mechanisms occurring around the crack tip. Those that occur in front of the crack tip, termed intrinsic mechanisms, contribute significantly to fracture toughness — plasticity accounts for up to 95% of fracture toughness in ductile metals [15,16]. And those that occur behind, termed extrinsic mechanisms, while contributing little to the fracture toughness, are the only relevant ones in quasi-brittle materials like composites [11,15]. Extrinsic mechanisms act in a localised region, primarily in the crack wake and require a pre-existing crack to be able to exert any influence, hence, they do not affect crack initiation toughness (see Fig. 2a).

This split of fracture toughness into remote work of plastic deformation and local work of separation corresponds to the Turners' interpretation of tearing resistance [17], which has been used to understand the origins of the total fracture toughness in different materials [16,18–23].

The objective of this work is to clarify the effect pseudo-ductility has on the toughness and nominal strength of quasi-isotropic composite laminates. The analysis is numerical and relies on a user-defined material model representing pseudo-ductility (Section 2.2 and Appendix A). The simulation of Compact Tension (CT) coupons provides information on the translaminar toughness associated to the pseudo-ductile constitutive model depending on its parameters (Section 4). The constitutive model allows also to estimate the nominal strength of Centre-Crack (CC) specimens (Section 4.2). In this case, we explore the size-effect by scaling the specimens for a fixed crack length to width ratio (R/W). Furthermore, we discuss the nominal strength limits of CC specimens (for small and large specimens) using the fracture toughness information obtained from CT specimens.

2. Numerical approach

2.1. General aspects

Depending on the desired scales of damage representation, two different approaches exist to numerically characterise a pseudo-ductile laminate: mesoscale (lamina level) and macroscale (laminate level). Mesoscale approaches are considered if ply-level pseudo-ductile damage mechanisms are desired. We disregard mesoscale models with the capability to capture fragmentation and dispersed delamination, as they are cumbersome to generate and are computationally expensive, especially in the light of our objective to capture the size effect. The interested reader is referred to [12] for mesoscale modelling of pseudo-ductile laminates.

On the other hand, pseudo-ductile composite laminates can also be considered as a homogeneous equivalent material, generally referred to as a macroscale (laminate) level approach. With constitutive models relating the stresses and strains, fragmentation could nucleate from a smooth surface without pre-crack, similar to metal plasticity. However, the pseudo-ductile damage mechanisms (fragmentation, dispersed-delamination and fragmentation saturation) are only reflected as stiffness reduction in the global laminate response (i.e., lamina-level stress distribution is unavailable). We chose the macroscale approach since it allows for rapid evaluation of different successful pseudo-ductile laminate configurations. Furthermore, macroscale approaches only require the eventual stress–strain response (see Fig. 1, Fig. 2b) brought on by the pseudo-ductile material. Macroscale pseudo-ductile representation also dovetails with our objective to vary the proportion of energy dissipation by different damage mechanisms (intrinsic and extrinsic). i.e., to determine the influence of pseudo-ductility.

Considering pseudo-ductility as an intrinsic dissipation through a macroscale continuum approach is only valid when there is a sufficient difference in scale between the various damage mechanisms. Three associated lengths characterise these mechanisms: fibre fragmentation length, ply fragmentation length, and the Fracture Process Zone (FPZ) length (ℓ_{FPZ}). Both fibre and ply fragmentation lengths decrease with the increase in strain (due to the increase in density); thus, a direct comparison of these lengths is inappropriate. At saturation, however, there is a notable difference in scale; for instance, fibre fragmentation lengths typically range between 0.3–0.4 mm [24], while ply-fragmentation lengths range between 1–3.5 mm [1,12]. Meanwhile, FPZ lengths (ℓ_{FPZ}) are significantly larger than ply-fragmentation lengths, typically ranging between 6–10 mm [25].

2.2. Idealised pseudo-ductile constitutive model

We consider a homogenised quasi-isotropic pseudo-ductile laminate under plane-stress loading with only in-plane damage mechanisms. The model defines the uniaxial stress–strain response with two lines, see Fig. 2b. In the elastic zone, prior to yield ($\varepsilon < \varepsilon_y$), the slope is elastic modulus (E), while in the pseudo-ductile regime it reduces to hE ($0 < h < 1$). The response can be traced to the origin with a reduced slope during unloading: $m_i E$, where m_i is the integrity initialised to 1. Once the stress at the crack tip reaches the material strength (σ_f), the crack opens ($\omega > 0$), as the cohesive elements are implemented in "series". See Appendix A for detailed explanation on the constitutive material model.

The FPZ for a pseudo-ductile material includes a softening zone linked to the quasi-brittle behaviour of the material (extrinsic dissipation mechanism) and a hardening region linked to the intrinsic dissipation mechanism (Fig. 2a). The creation of a new crack surface is widely represented by a cohesive zone model, governed by the cohesive law, which is considered a material property and relates the crack opening stresses with the crack opening displacement, $\sigma(\omega)$. We have chosen linear cohesive law, characterised by two material parameters (σ_f and $\mathcal{G}_{Ic}$) and a numerical penalty stiffness ($\tilde{K}$). In this case, σ_f is the material strength that defines the failure onset and the area under the stress-crack opening curve is the fracture energy ($\mathcal{G}_{Ic}$), Fig. 2c. Although other cohesive law profiles (trilinear, exponential, etc.) may better represent the specific behaviour of composites or concrete [11,26], we selected a linear degradation. The initial stiffness ($\tilde{K}$) of an ideal cohesive law should be infinite. However, a finite value is required to ensure the stability of the Finite Element Model (FEM), and it should be chosen such that the structures' initial compliance remains unaffected [27].

Thus, the material properties of the model considering a quasi-isotropic pseudo-ductile laminate are $E, \nu, \varepsilon_y, \varepsilon_f$ for the continuum material, and $\sigma_f, \mathcal{G}_{Ic}$ for the cohesive law. These pseudo-ductile material parameters (σ_f, σ_y, H) can be obtained from a single unnotched tensile test. We acknowledge that the response of some pseudo-ductile materials [4,5] deviates from linearity, and a linear fit may not accurately represent their behaviour. However, we restrict ourselves to a linear response (Fig. 2b), as it reduces the problem complexity by reducing the number of non-dimensional parameters involved in the model.

3. Methodology

3.1. Non-dimensional analysis and design of experiments

The fracture energy, $\mathcal{J}$, for a pseudo-ductile quasi-isotropic material can be adequately characterised by the parameters of the constitutive model (Fig. 2),

$$\mathcal{J} = f\left(E, \sigma_y, \varepsilon_d, \sigma_f, \omega, \mathcal{G}_{Ic}\right) \tag{1}$$

We follow the principles of dimensional analysis – Buckingham π theorem [28] – to reduce the problem complexity considering a given geometry and loading. The dimensional analysis states that any physically meaningful system with n independent parameters can equivalently be rewritten as $n - m$ dimensionless parameters, where m is the number of primary dimensions [28]. Here, we have six independent parameters (Eq. (1)), which contains only two primary dimensions: Force (N) and length (L), as the problem is not time dependent. Thus, for a growing crack, we have four non-dimensional variables: $\varepsilon_y, \varepsilon_d, \sigma_f/\sigma_y$ and $\sigma_f\omega/2\mathcal{G}_{Ic}$. Prior to the steady state (i.e., during the FPZ development) the normalised dissipated energy, $\tilde{\mathcal{J}} = \mathcal{J}/\mathcal{G}_{Ic}$, grows with the normalised crack opening ($\tilde{\omega} = \sigma_f\omega/2\mathcal{G}_{Ic}$). However, $\tilde{\omega}$ tends to 1 at steady-state ($\omega = \omega_c$), since $\mathcal{G}_{Ic} = \left(\sigma_f\omega_c\right)/2$ for a linear cohesive law. Thus, the normalised steady-state energy release rate ($\mathcal{J}^{ss}/\mathcal{G}_{Ic}$) is dependent on only three non-dimensional parameters characterising the pseudo-ductile material. Though the choice and the form of the non-dimensional parameters are infinite, these combinations (Eq. (2)) are generally chosen for their physical meaningfulness [16,19,20]. Accordingly,

$$\frac{\mathcal{J}^{ss}}{\mathcal{G}_{Ic}} = f_{ss}\left(\varepsilon_y, \varepsilon_d, \frac{\sigma_f}{\sigma_y}\right) \tag{2}$$

The influence of yield strain (ε_y) in Eq. (2) has been shown to be negligible [16,23], although, $\sigma_y\left(= E\varepsilon_y\right)$ itself has major influence through σ_f/σ_y. We have numerically verified its insignificance. Specifically, by defining several models with constant ε_d and s_H, we observed only a relatively minor influence on $\mathcal{J}^{ss}$. So, we concentrated (Fig. 4) on (i) the effect of the pseudo-ductile strain, ε_d, while keeping the ratio between strength and yield stresses, $s_H = \sigma_f/\sigma_y$, constant (ε_{di} study), and (ii) the effect of s_H, while keeping ε_d constant (s_{Hi} study).

Typical quasi-isotropic pseudo-ductile laminate properties were considered, $E_1 = E_2 = 25$ GPa (e.g., pseudo-ductile glass–carbon–glass quasi-isotropic laminate [7]) and $\mathcal{G}_{Ic} = 75$ N mm^{-1} and a pseudo-yield strain (ε_y) of 1.25% (σ_y=312.5 MPa), for all the cases. For the ε_{di} study, s_H was fixed at 1.6 ($\sigma_f = 500$ MPa) and ε_{di} took the values of 0.75%, 1.75%, and 6.75% ($h = 0.5$, 0.3, and 0.1) to explore a wide range of pseudo-ductility, Fig. 4a. Higher pseudo-ductile strains (> 7%) were not considered as the associated failure strains are unrealistically large (> 10%). A pure linear elastic case ($\varepsilon_d = 0, \varepsilon_y = \varepsilon_f = 2\%, \sigma_f = 500.0$ MPa) was included in the study to validate the FE model against existing Linear Elastic Fracture Mechanics (LEFM) solutions.

Similarly, for the s_{Hi} study, ε_d was kept constant at 6.75% (Fig. 4b); the highest ε_d considered in the ε_{di} study. Previous studies have revealed that the parameter, s_H, is the most influential on toughness in metals under plane-strain [16,20,23]. We selected s_H of 1.075, 1.3, 1.6, 1.8 and 2.0. The case s_{H1} of 1.075 can be thought of as a near perfectly pseudo-ductile material, with no hardening.

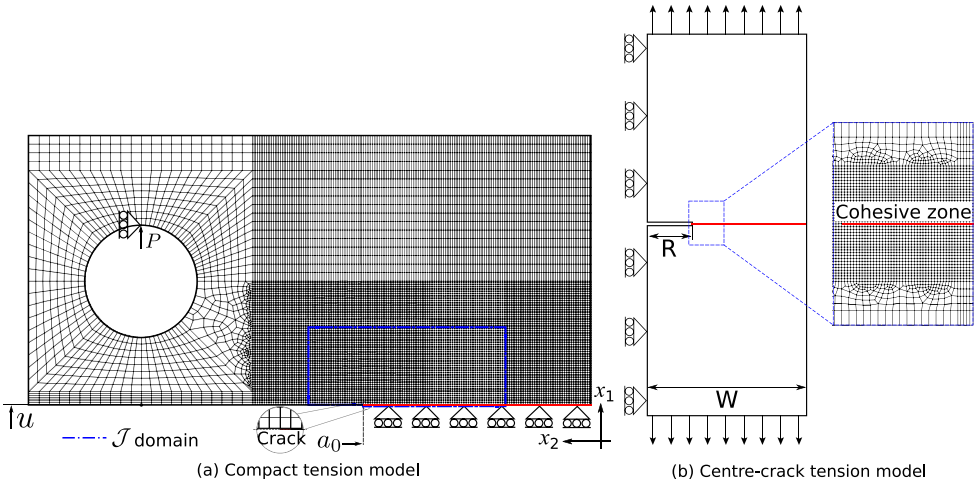

Fig. 3. Schematic of Finite Element models. (a) Half-symmetric compact tension model. Dashed blue lines represent the $\mathcal{J}$-integral domain and a_0 is the initial crack-tip position. (b) Schematic of a half-symmetric centre-crack FE model under tension. Zoomed region represents the mesh around the crack-tip.

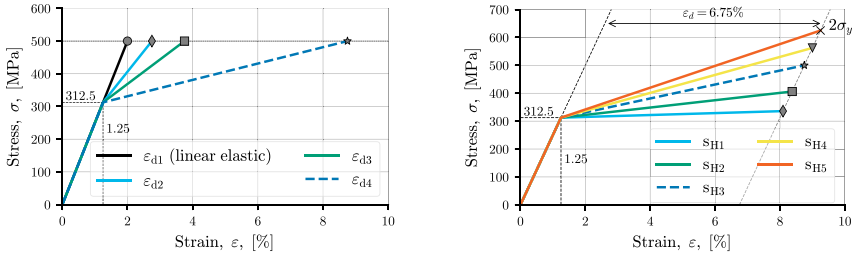

Fig. 4. Design of experiments for the quasi-isotropic pseudo-ductile stress–strain response. (a) ϵ_{di} study with constant s_H=1.6, (b) s_{Hi} study with constant $\epsilon_d = 6.75\%$. Note that ϵ_{d4} and s_{H3} are equivalent.

3.2. Extracting dissipated energy during crack extension

The dissipated energy during crack extension in the CT model was computed using the $\mathcal{J}$-integral [29]. As the $\mathcal{J}$-integral is an accumulated quantity, similar to the rising $\mathcal{R}$-curve, it includes the contribution from both the intrinsic and extrinsic mechanisms [17]. Therefore, the steady-state dissipated energy ($\mathcal{J}^{ss}$) during crack extension is given by,

$$\mathcal{J}^{ss} = \mathcal{J}_{CL} + \mathcal{J}_{pd} \tag{3}$$

where $\mathcal{J}_{CL}$ is the dissipated energy corresponding to the extrinsic mechanisms defined by the cohesive law (also referred to as $\mathcal{G}_{Ic}$), and $\mathcal{J}_{pd}$ is the contribution to the dissipated energy from the intrinsic mechanisms (pseudo-ductility). Similar ideas have been used to systematically analyse the parameters influencing the intrinsic and extrinsic dissipation mechanisms in different materials [16,20–23]. In this study, we intend to analyse the influence of the energy associated with pseudo-ductility, $\mathcal{J}_{pd}$, on $\mathcal{J}^{ss}$. The intrinsic dissipation, $\mathcal{J}_{pd}$, is varied indirectly by the parameters governing the pseudo-ductile region of the constitutive material (see Fig. 1). Therefore, the increment of material toughness of a pseudo-ductile material over that of a merely quasi-brittle material is quantified by the ratio $\mathcal{J}^{ss}/\mathcal{G}_{Ic}$.

3.3. FE models to extract translaminar toughness and nominal strength

We used Compact Tension models to analyse the effect of pseudo-ductility on translaminar toughness and to extract the corresponding $\mathcal{J}-\omega$ curves. In turn, the effect of the obtained fracture toughness ($\mathcal{J}$-curves) on nominal strength was assessed with Centre-Crack specimens of different sizes.

Fig. 3 shows the two-dimensional plane-stress model of the CT and the CC specimen and their boundary conditions. The constitutive model described in Section 2.2 and Appendix A was implemented as a user material model (UMAT subroutine). We used the built-in traction-separation based cohesive law with the 4-noded planar cohesive element (COH2D4) available in Abaqus (version 6.14). Finite thickness cohesive elements were placed along the *a priori* crack path to aid in the visualisation of the damage rather than the zero-thickness cohesive elements.

Fig. 3a highlights the path to compute the $\mathcal{J}$-integral in the CT specimens. It was evaluated using the built-in *CONTOUR INTEGRAL (contours = 5) function of Abaqus. To assure the path independence of the result [29,30], the path was conceived large enough to contain the pseudo-ductile zone and to assure that the path edges parallel to x_2 pass only through elastic stresses [16]. Furthermore, contour independence was verified by the convergence of the energy release rate in the contours.

Due to the bending dominated response in CT models, especially at the back end, we used reduced integration elements (CPS4R) to avoid the artificial bending stiffness introduced by fully integrated elements (CPS4). CPS4 elements were used in CC models as bending, in this case, is negligible. This selection for CC facilitated the simulation of large specimens with large elements that are required for the size-effect study (reduced integration elements would require finer meshes).

The geometry of the CT specimen was taken from the corresponding standard for metals (ASTM E1820 [31] or ASTM E399 [32]) as there is no standard test for the measurement of the translaminar fracture toughness in composites. This is a common selection in the composites field [33,34]. The width, W, was of 51 mm and the initial crack length, a, 26 mm ($a/W = 0.51$) with a pinhole diameter of 12.75 mm ($0.25W$). Symmetric boundary conditions were assumed to take advantage of the geometric symmetry, depicted in Fig. 3a. As the crack ligament is situated on the symmetry plane, only half the fracture energy is required. Cohesive elements with only one constrained face exhibit singular modes due to the lack of membrane stiffness [35]. To avoid the propagation of these modes, x_1 degree of freedom ($x_1 = 0$) of a single node was constrained at the end. It is stated that the different pin-hole loading configurations such as uniformly distributed, radially distributed or point load, have insignificant effects on the specimen compliance for $a/W > 0.4$ [36]. Therefore, we used a kinematically constrained reference point at the pin-hole to apply the controlled displacement and recorded the resultant vertical reaction forces.

Centre-crack (CC) specimen FE models, Fig. 3b, consisted of half-symmetric 2D plane stress models with fully integrated elements (CPS4). As in CT, we placed a row of cohesive elements along the crack propagation path but, in this case, we used the complete fracture toughness. Due to the non-linear dynamic nature of the CC case, we used the implicit solver with direct integration (*DYNAMIC, APPLICATION=TRANSIENT FIDELITY). A fixed boundary condition was applied to the bottom edge ($x_1 = 0$), whereas the top edge was loaded with controlled displacement in x_1 direction. To study the size-effect and determine the strength limits for small and large coupons, we varied the half-notch lengths (R) from 0.2 to 160 mm, while maintaining the width to radius ratio: $R/W = 1/6$. We generated different meshes for each specimen width. To properly characterise the FPZ, element size was defined following [27]. A mesh convergence study ensured sufficient element size in models without pseudo-ductility, and are then scaled correspondingly for pseudo-ductile models. Finally, we employed a two-way bias (from the notch) towards both edges to minimise element count.

4. Results

4.1. Effect of pseudo-ductility on fracture toughness

To validate the numerical approach, we compared the load–displacement (P-u) response of the linear elastic material (case ϵ_{d1}) to the handbook solution for isotropic materials [37]. The agreement in the initial stiffness and degradation response was good (Fig. 5). The other cases, Fig. 5a and Fig. 5b, indicate that an increase in pseudo-ductility entails an increase in the peak load and its corresponding displacement.

The normalised fracture toughness ($\bar{\mathcal{J}} = \mathcal{J}/\mathcal{G}_{Ic}$) increases monotonically with the normalised crack opening ($\bar{\omega} = \sigma_f \omega / 2\mathcal{G}_{Ic}$) during the FPZ development until it reaches a plateau (Fig. 5c and Fig. 5d). For the linear-elastic material (case ϵ_{d1}), $\bar{\mathcal{J}}$ reaches the steady-state value of 1 ($\bar{\mathcal{J}} = 1, \bar{\omega} = 1$) because the dissipated energy is completely contributed by the cohesive traction. All the cases involving pseudo-ductility exhibit $\bar{\mathcal{J}} > 1$ due to the contribution of the intrinsic damage mechanism and the steady-state is also achieved at $\bar{\omega} > 1$. In other words the difference, $\left[\bar{\mathcal{J}}(\bar{\omega})\right]_{\epsilon_{di}} - \left[\bar{\mathcal{J}}(\bar{\omega})\right]_{\epsilon_{d1}}$, represent the total intrinsic energy dissipated as the crack grows. Cases ϵ_{d4} and s_{H5} improve the $\mathcal{J}^{ss}$ the most, as suggested by the P-u curves and substantiated by the $\mathcal{J}_\omega$ curves.

Fig. 6A, corresponding to the case ϵ_{d4}, illustrates the contribution of pseudo-ductility to the increase in fracture energy at the different stages of crack growth. The pseudo-ductile zone shapes in Fig. 6A a, c, e and g denote the damage contour in the x_1 direction provided by the integrity function of the constitutive model and, similarly, Fig. 6A b, d, f and h that of the x_2 direction. At the initiation of crack growth ($\bar{\omega} \approx 1$) the pseudo-ductile zone takes the characteristic "butterfly" shape (Fig. 6A c), and then the radius of the pseudo-ductile zone increases with crack growth until steady-state conditions are achieved (Fig. 6A). The dissipated energy in this pseudo-ductile zone, accounts for the observed increase in fracture toughness $\bar{\mathcal{J}}$. During steady-state crack growth, the pseudo-ductile zone radius ahead of the crack tip stays constant, leaving a pseudo-ductile wake.

The steady-state $\mathcal{J}$-integral provides the maximum available toughening effect for a pseudo-ductile material as it results from the contribution of all the micro-mechanisms involved, once fully developed. Its normalisation to the cohesive energy, $\bar{\mathcal{J}}$, reveals the energy dissipated by the pseudo-ductile work in the surrounding material. In the ϵ_{di} study, $\bar{\mathcal{J}}$ increases near linearly with the pseudo-ductile strain while keeping the normalised traction strength (s_H) constant at 1.6 (Fig. 7a). We can readily attribute this increment to pseudo-ductile dissipation in the material surrounding the crack ligament. The increase of the pseudo-ductile strain, ϵ_d, enlarges the intrinsic dissipation zone and raises the steady-state resistance (top row of Fig. 6B and Fig. 7a).

The increase of $\bar{\mathcal{J}}$ with the normalised strength, s_{Hi} study, is highly non-linear (Fig. 7b). The increase in fracture toughness relates to the need to attain higher stresses ahead of the crack tip as the crack advances. The case s_{H1} ($s_H = 1.075$) can be considered as a near perfect pseudo-ductile case ($s_H = 1$) where no increase in fracture toughness is expected ($\bar{\mathcal{J}}$=1) because the pseudo-ductile zone would be confined in the crack plane. Though the overall size of the pseudo-ductile (or intrinsic) zone is similar, the size of the most intense region (the region near the crack-tip) decreases with increasing s_H (bottom row of Fig. 6B). Another noticeable feature in the pseudo-ductile zone shapes is the decreasing length of the cohesive zone. This is a consequence of the definition of the investigation which considers $\mathcal{G}_{Ic}$ constant while varying the cohesive strength, σ_f, thus the critical crack opening (ω_c) is reduced as the ratio of s_H increases.

For the s_{Hi} study (constant ϵ_d of 6.75%), and in spite of the relative increase in strain energy under the stress–strain curves (1.14, 1.34, 1.49 and 1.64 times the s_{H1} case), the toughening effect ceases at $s_H \approx 1.6$. Similar s_H dependency on crack growth resistance has also been demonstrated by others [16,20,23].

We expect the presented $\mathcal{J}^{ss}$ trends to be valid for other combinations of parameters, as the fracture process is characterised by the significant non-dimensional parameters (Eq. (2)). We illustrate this statement in Appendix B by repeating the process outlined in Section 3.

4.2. Effect of pseudo-ductility on strength

To investigate the influence of pseudo-ductility on the nominal strengths (σ_N) of semi-structural specimens; we use the centre-cracked FE models developed in Section 3.3 to extract the nominal strengths, defined as the ultimate load (F_u) to the net section area (A).

$$\sigma_N = \frac{F_u}{A} = \frac{F_u}{2(W-R)t} \tag{4}$$

Depending on the specimen size, two extreme responses are expected when a notched quasi-brittle material fails. For small specimens, failure is ductile, and the nominal strength tends to σ_f (un-notched strength limit). On the other hand, for extremely large centre-cracked specimens, a brittle failure (elastic limit) is expected, in which the strength continues to be reduced with the specimen size according to LEFM, given by,

$$\frac{\sigma_N}{\sigma_f} = \sqrt{\bar{\ell}_{\mathrm{SEL}}} = \sqrt{\frac{\ell_M}{RF^2}} = \sqrt{\frac{E\mathcal{G}_{Ic}}{RF^2\sigma_f^2}} \tag{5}$$

where $\bar{\ell}_{\mathrm{SEL}} (= \ell_M/RF^2)$ is the FPZ length normalised by the notch radius, $\ell_M (= E\mathcal{G}_{Ic}/\sigma_f^2)$ is the material characteristic length relating

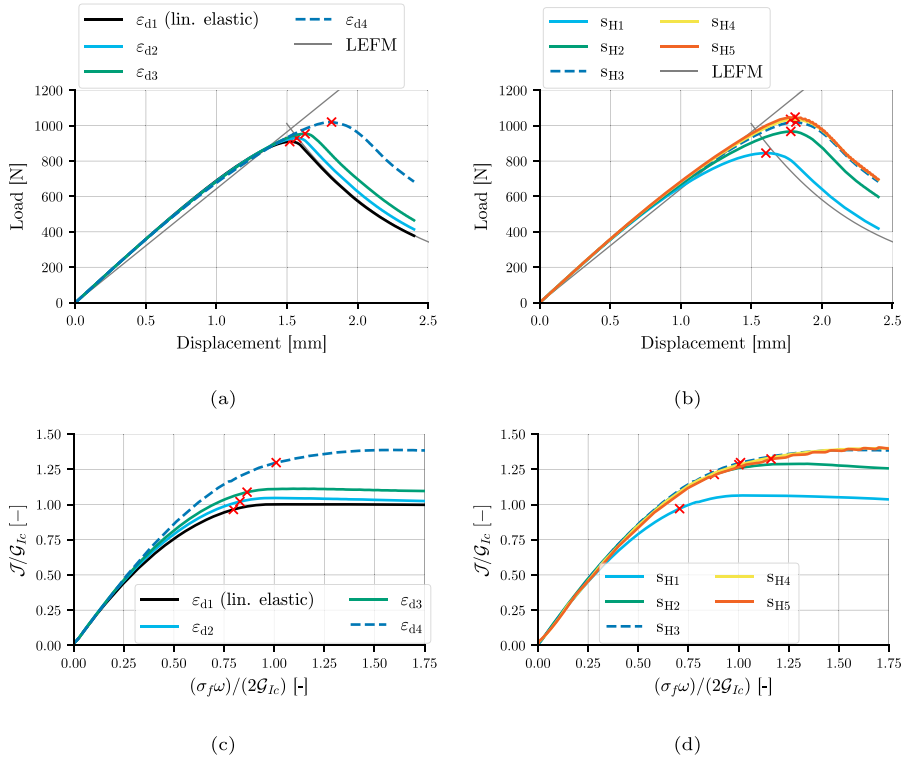

Fig. 5. Load–displacement response of compact tension specimens for ϵ_{di} study (a) and s_{Hi} study (c). Corresponding normalised energy release rate behaviour, $\mathcal{J}$-integral ($\mathcal{J}/\mathcal{G}_{Ic}$) for ϵ_{di} (b) and s_{Hi} study (d). The cross markers represent the peak load in (a) and (c) and the crack opening corresponding to peak load in (b) and (d). Note that ϵ_{d4} and s_{H3} are equivalent.

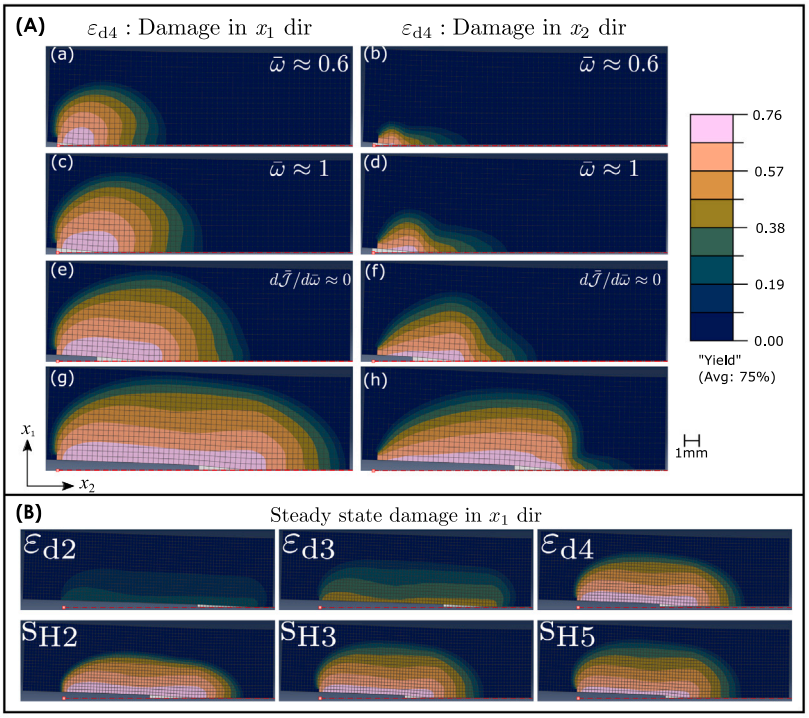

Fig. 6. Pseudo-ductile zone shapes: (A) Pseudo-ductile-zone growth at different stages for ϵ_{d4} and (B) steady-state pseudo-ductile zone shapes for selected cases. (a) and (b) are prior to any traction-free crack growth ($\Delta a = 0$), (c) and (d) at the critical crack opening, (e) and (f) at the steady-state and (g) and (h) are past the steady-state.

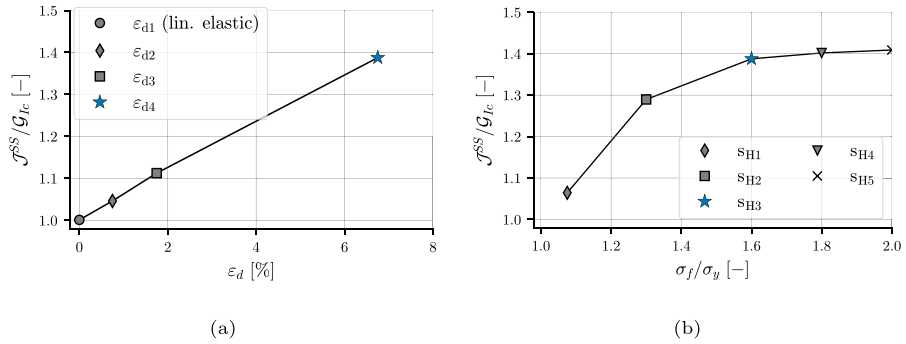

(a) (b)

Fig. 7. Normalised steady-state energy release rate $(\bar{J}^{ss} = J^{ss}/\mathcal{G}_{Ic})$ for (a) ε_{di} study and (b) s_{Hi} study. Note that ε_{d4} and s_{H3} are equivalent.

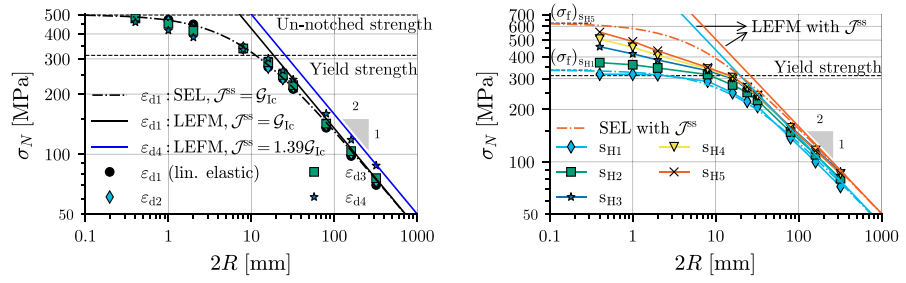

(a) ε_{di} study (b) s_{Hi} study

Fig. 8. Nominal centre-crack tension strengths for ε_{di} and s_{Hi} study. Dotted and solid lines correspond to Bažant Size Effect Law (Eq. (7)) and LEFM (Eq. (5)) estimates, respectively. Fracture toughness in both SEL and LEFM are substituted with corresponding $\mathcal{J}^{ss}$ from compact tension results (Fig. 7). Note that ε_{d4} and s_{H3} are equivalent.

translaminar fracture toughness, elastic modulus and the ultimate material strength, and F is the geometric correction factor to account for finite geometric effects [37], given by,

$$F = \left[1 - 0.025\left(\frac{R}{W}\right)^2 + 0.06\left(\frac{R}{W}\right)^4\right]\sqrt{\sec\left(\frac{\pi R}{2W}\right)} \tag{6}$$

where, R/W is the ratio of notch radius to specimen width.

The Bažant Size Effect Law (SEL) defines the asymptotic relationship between both extremes (un-notched strength and LEFM limit) for geometrically similar structures [38,39]. The nominal strength of cracked specimens is provided by [38],

$$\frac{\sigma_N}{\sigma_f} = \sqrt{\frac{\bar{\ell}_{\text{SEL}}}{1 + \bar{\ell}_{\text{SEL}}}} \tag{7}$$

We present the nominal strengths in a bi-logarithmic scale (Fig. 8) since the nominal strength at the elastic limit and specimen size has a linear relationship with a slope of −1/2 for quasi-brittle materials [40,41]. We can observe that the nominal strengths of the linear-elastic specimens (ε_{d1}) tend towards the expected asymptotes, i.e., elastic limit on the one hand ($R \to \infty$) and un-notched strength on the other hand ($R \to 0$), validating the developed FE models (Fig. 8a). Additionally, for the linear elastic specimens, the Bažant SEL (Eq. (7)) predicts well the σ_N for the entire range of specimen sizes considered.

Regarding the effect of pseudo-ductility on nominal strength, we expect that the initially sharp crack tip will blunt, followed by the elastic unloading and crack growth, as in any elastic–plastic material. These tip blunting and crack extension mechanisms are terminated by either specimen failure or when the entire failure plane is in the pseudo-ductile region ($\varepsilon_d > 0$). We anticipate this crack growth mechanism will result in increased nominal strength, which is observed, for example, for specimens with $2R = 320$ mm: σ_N of ε_{d4} is 25% more than that of ε_{d1} i.e., $(\sigma_N)_{\varepsilon_{d4}}$ is 87.68 MPa, whereas $(\sigma_N)_{\varepsilon_{d1}}$ is 70.09 MPa, Fig. 8a. However, on the other extreme (small specimen sizes) the nominal strength decreases with increasing pseudo-ductility: up to −14% from ε_{d1} to ε_{d4}, i.e., $(\sigma_N)_{\varepsilon_{d4}}$ is 384.35 MPa whereas $(\sigma_N)_{\varepsilon_{d1}}$ is 446.9 MPa for $2R = 2$ mm, Fig. 8a.

For a given crack length, the elastic limit of the linear elastic material is determined by the fracture toughness (Eq. (5)). We hypothesise that the elastic limit of a pseudo-ductile material could easily be estimated by considering the steady-state toughness obtained from the CT specimens (Fig. 7). The accordingly updated elastic limit is shown for ε_{d4} in Fig. 8a.

We observe similar nominal strength responses for all the pseudo-ductile cases studied (s_{Hi} and ε_{di}). That is: increased σ_N for large pseudo-ductile specimens, reduced σ_N for intermediate specimens, and $\mathcal{J}_{ss}$ capturing the LEFM limit for pseudo-ductile specimens.

However, the intermediate pseudo-ductile specimens – $R < EJ_{ss}/\sigma_y^2 F^2$ – present a smaller strength than their linear-elastic counterpart. Pseudo-ductility, manifesting as damage post-yielding, reduces strength due to the decreased effective stiffness in the failure plane. Considering pseudo-ductile material (ε_{d4}, material B in Fig. 9a), we can compare it with two linear-elastic materials, A and C, with distinct elastic moduli. Material A represents a linear-elastic material based on the initial modulus (E), while Material C, also linear-elastic, is based on the secant modulus ($E_S = \sigma_f/\varepsilon_f$), as illustrated in Fig. 9a. Fig. 9b displays FE results of the notched strength for pseudo-ductile material (B) alongside SEL (Eq. (7)) for materials A and C. For larger specimens, SEL for material A aligns closely with FE results for material B since the material remains predominantly in the elastic regime. As specimen size decreases, FE results start to diverge, and for very small specimens, they closely match SEL for material C. This is due to the stress in the failure plane approaching σ_f, resulting in reduced effective stiffness.

This intermediate behaviour will be further evident if one normalises the nominal strength of all the cases by their corresponding failure strength (σ_N/σ_f) and present against the $\bar{\ell}^{-1}_{\text{SEL}}$. This suggests the existence of an intermediate asymptotic behaviour that is typical of the plastic-hardening materials [42,43], which could be characterised by incorporating the modulus variation past yield (like secant modulus) in the SEL (Eq. (7)).

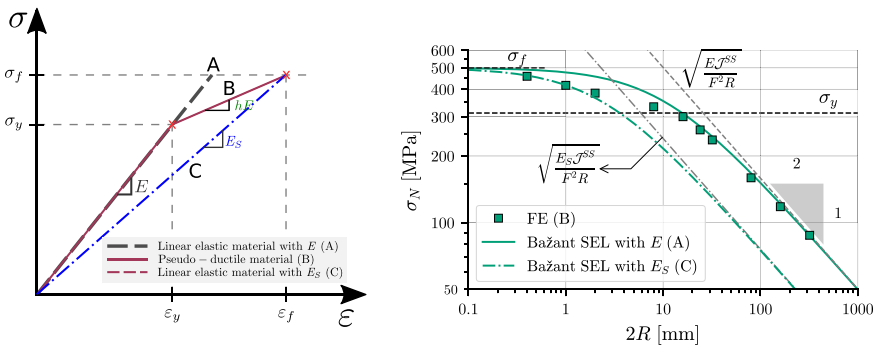

(a) (b)

Fig. 9. Schematic representation of different moduli and the nominal strength estimates of centre-cracked specimens according to Bažant Size Effect Law (Eq. (7)) and LEFM (Eq. (5)) for ε_{d4} using elastic (E) and secant modulus ($E_S = \sigma_f/\varepsilon_f$).

5. Discussion

The pseudo-ductile damage mechanisms initiate from a smooth surface and evolves stably prior to the pre-crack growth. However, the pre-crack (macro-crack) is inevitably forced to grow across this damaged region upon fragmentation saturation (that may deviate from the straight path as assumed here). Thus, pseudo-ductility is not *a priori* independent of extrinsic dissipation. The incorporation of pseudo-ductility will encourage intrinsic dissipation mechanisms, but it may also detrimentally affect the extrinsic mechanisms. Consequently, the normalisation of total fracture toughness by a constant extrinsic energy – as in Fig. 7 – might be improper. This is a potential limitation of the adopted approach (macroscale continuum representation of pseudo-ductility), which could only be rectified through mesoscale (lamina level) modelling, as defined in Section 2.2.

Though we observe a positive pseudo-ductile influence on translaminar toughness (Fig. 7), the experimental evidence is both contradictory and difficult to attribute to pseudo-ductility alone. Ply-blocking of low and high elongation plies to form sublaminates is the typical way to achieve pseudo-ductility [1,7], see Fig. 1b. However, this makes the interpretation of improvements in translaminar toughness difficult, as the $\mathcal{G}_{Ic}$ is shown to increase linearly with increasing ply thickness — due to the reducing stress concentration factor and other notch blunting mechanisms [44,45]. For instance, Danzi et al. [46] attributes the translaminar toughness improvement to the thickness effect rather than pseudo-ductility in ply-blocked cross-ply pseudo-ductile laminates (from double-edge notched specimens). On the contrary, translaminar toughness improvements can be attributed to pseudo-ductility in the non ply-blocked quasi-isotropic pseudo-ductile laminates of Cugnoni et al. [10] (from CT specimens).

Meanwhile, the experimental evidence available on the pseudo-ductile centre-cracked specimens is insufficient to compare with the presented results for two reasons. One, the nominal strengths from a single specimen size are inadequate to characterise the size-effect behaviour – [5,6] tested only on single notch radius ($2R = 3$ mm). Secondly, the smaller width specimens (as in [5,6]) are particularly inappropriate for notch sensitivity experiments since the ℓ_{FPZ} spans most of the specimen width resulting in nominal strengths closer to the un-notched strength.

Maximum possible pseudo-ductile strain in a ply-blocked pseudo-ductile laminate is the difference between failure strain and yield strain, i.e., an elastic perfectly pseudo-ductile material ($h \approx 0, \sigma_f/\sigma_y \approx 1$). These failure and yield strain nearly correspond to the failure strain of high and low strain material; thus, they must be maximised accordingly. Though linear perfectly pseudo-ductile laminate is the optimum configuration in terms of pseudo-ductile behaviour, our results (Figs. 7, 8 and B.10) indicate that the perfect pseudo-ductile material is not the optimal in terms of toughness and strength. Thus, maximising the pseudo-ductile strain for a quasi-isotropic laminate with strength ratios > 1 (around 1.5) makes a better overall trade-off.

6. Conclusions

Within the framework of the current interest to impart pseudo-ductility to composite materials, we have presented a numerical study to elucidate how pseudo-ductility affects material toughness, and the nominal strength of centre cracked specimens. We first presented a constitutive pseudo-ductile model and its implementation in a Finite Element environment. Then, we introduced the design of experiments on the effect of the two most important non-dimensional parameters – pseudo-ductile strain (ε_d) and ratio between strength and pseudo-yield stress (σ_f/σ_y) – on the normalised fracture toughness.

The fracture toughness of the pseudo-ductile materials was predicted using numerical simulations of the Compact Tension specimen. These revealed a near linear relationship between toughness and the pseudo-ductile strain, whereas the dependence with the strength ratio was highly non-linear: a steep rise followed by a plateau. They also revealed that the ideal pseudo-ductile conditions, near-perfect plastic, ($\varepsilon_d > 0, \sigma_f/\sigma_y \approx 1$) do not improve fracture toughness.

Then, we concentrated on simulating the nominal strength of centre-cracked specimens. In the elastic limit extreme (large specimens) pseudo-ductility improved the nominal strength by up to 26% in comparison to the linear-elastic case (for the considered parameters). Moreover, the elastic limit tendency could be captured if the corresponding translaminar fracture toughness from the CT specimens was accounted for. The nominal strength of specimen sizes lying in the intermediate region between ductile and elastic limit was below the values predicted by the Size Effect Law, SEL (up to −14%).

CRediT authorship contribution statement

A. Subramani: Conceptualization, Methodology, Software, Visualization, Writing – original draft, Writing – review & editing. **P. Maimí:** Conceptualization, Funding acquisition, Resources, Supervision, Validation, Writing – review & editing. **J. Costa:** Funding acquisition, Resources, Supervision, Writing – review & editing.

Declaration of competing interest

The authors declare that they have no known competing financial interests or personal relationships that could have appeared to influence the work reported in this paper.

Data availability

No data was used for the research described in the article.

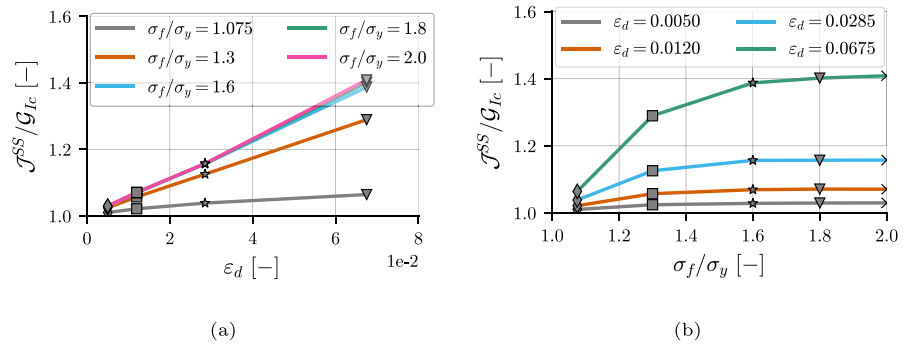

Fig. B.10. Normalised steady-state energy release rate $(\bar{J}^{ss} = J^{ss}/\mathcal{G}_{Ic})$ for (a) ε_{di} study and (b) s_{Hi} study. Note that ε_{d4} and s_{H3} are equivalent.

Acknowledgements

The authors greatly acknowledge the funding and support of Ministerio de Ciencia, Innovación y Universidades, Spain for the project *En pos de materiales compuestos de fibra larga híbridos, bio-basados y sostenibles para aplicaciones estructurales* (SUBHYCO) (PID2021-126989 OB-I00). Anbazhagan Subramani acknowledge the financial support of Universitat de Girona, Spain for INV309_2019 and also likes to thank Universitat de Girona and Santander Universidades for the financial resources provided through *Personal Investigador en formaciò* (IF_UDG), 2020. Open Access funding provided thanks to the CRUE-CSIC agreement with Elsevier.

Appendix A. Constitutive model to characterise pseudo-ductility

The complementary Gibbs free energy density (Ψ) of an idealised quasi-isotropic pseudo-ductile laminate (as in Fig. 2b) under isothermal conditions is postulated as follows [47]

$$\Psi := \frac{1}{2E}\left(\frac{\sigma_{11}^2}{m_1} + \frac{\sigma_{22}^2}{m_2} - 2\nu\sigma_{11}\sigma_{22} + 2\sigma_{12}^2\left[\frac{1+\nu\sqrt{m_1\, m_2}}{\sqrt{m_1\, m_2}}\right]\right) \tag{A.1}$$

where E and ν are respectively the elastic modulus and the Poissons' ratio of the undamaged material. m_1 and m_2 are integrity functions (the damage evolution need not necessarily be isotropic) with an initial value of 1, which decrease with degradation. Note that the shear modulus (G) is incorporated in Eq. (A.1), as $E\sqrt{m_1 m_2}/2(1+\nu\sqrt{m_1 m_2}) = G$. From Ψ, it is possible to obtain the strain tensor through Clausius–Duhem inequality [48] as:

$$\varepsilon = \frac{\partial\Psi}{\partial\sigma} = \mathbb{H}\sigma \quad \text{where:} \quad \mathbb{H} = \frac{1}{E}\begin{bmatrix} \frac{1}{m_1} & -\nu & 0 \\ -\nu & \frac{1}{m_2} & 0 \\ 0 & 0 & \frac{E}{G} \end{bmatrix} \tag{A.2}$$

where, $\mathbb{H}$ is the compliance tensor. The principal directions of damage are defined by two damage surfaces (longitudinal and transversal) using,

$$F_i = \sqrt{\langle\bar{\varepsilon}_{ii}\rangle^2 + \eta\bar{\varepsilon}_{12}^2} - \kappa_i - \varepsilon_y \leq 0 \quad \text{for } i = 1,2 \tag{A.3}$$

where k_1 and k_2 are internal variables that are initiated with 0, η is the shear contribution and set to 1 throughout. Scalar damage variables (d_i) with values between 0 (undamaged) and 1 (completely damaged) determine the integrity of the material point through, $m_i = 1 - d_i$. Functions, F_i, are computed in the principal strain directions when damage is zero and are latter frozen in the direction of damage. Then, the onset of degradation is the maximum principal strain criterion. The model is integrated as follows,

$$\kappa_i = \max_{s=0,t}\left\{\sqrt{<\bar{\varepsilon}_{ii}>^2 + \eta\bar{\varepsilon}_{12}^2}\right\} - \varepsilon_y \tag{A.4}$$

The integrity function is defined as:

$$m_i = \frac{H\kappa_i + \sigma_y}{E\kappa_i + \sigma_y} \text{ if } \kappa_i > 0 \tag{A.5}$$

where $H = (\sigma_f - \sigma_y)/(\varepsilon_f - \varepsilon_y)$ is the tangent modulus of the linear strain "hardening" region and $h = H/E$ is the "hardening" modulus ratio.

Appendix B. Generality of the translaminar toughness of pseudo-ductile materials

To verify the generality of the translaminar toughness presented in Section 4.1, we considered a complementary set of design-of-experiments similar to Section 3.1. We considered three additional logarithmically increasing pseudo-ductile strains (ε_d), 0.5%, 1.2%, and 2.85% with the same five strength ratios (s_H) ranging from 1.075 to 2, resulting in a total of 20 different pseudo-ductile materials. Following the procedure outlined in Section 3, we show that, indeed, both the $\bar{J}(\varepsilon_d)$ and $\bar{J}(s_H)$ presented in Fig. B.10 are general and follow similar trends as Fig. 7.

References

[1] Czél G, Wisnom MR. Demonstration of pseudo-ductility in high performance glass/epoxy composites by hybridisation with thin-ply carbon prepreg. Composites A 2013;52:23–30.

[2] Wisnom MR, Czél G, Swolfs Y, Jalalvand M, Gorbatikh L, Verpoest I. Hybrid effects in thin ply carbon/glass unidirectional laminates: accurate experimental determination and prediction. Composites A 2016;88:131–9.

[3] Czél G, Jalalvand M, Wisnom MR. Design and characterisation of advanced pseudo-ductile unidirectional thin-ply carbon/epoxy–glass/epoxy hybrid composites. Compos Struct 2016;143:362–70.

[4] Fotouhi M, Jalalvand M, Wisnom MR. High performance quasi-isotropic thin-ply carbon/glass hybrid composites with pseudo-ductile behaviour in all fibre orientations. Compos Sci Technol 2017;152:101–10.

[5] Czél G, Jalalvand M, Fotouhi M, Longana ML, Nixon-Pearson OJ, Wisnom MR. Pseudo-ductility and reduced notch sensitivity in multi-directional all-carbon/epoxy thin-ply hybrid composites. Composites A 2018;104:151–64.

[6] Fotouhi M, Jalalvand M, Wisnom MR. Notch insensitive orientation-dispersed pseudo-ductile thin-ply carbon/glass hybrid laminates. Composites A 2018;110:29–44.

[7] Fotouhi M, Jalalvand M, Saeedifar M, Xiao B, Wisnom MR. High performance quasi-isotropic thin-ply carbon/glass hybrid composites with pseudo-ductile behaviour loaded off-axis. Compos Struct 2020;247:112444.

[8] Fuller J, Wisnom M. Pseudo-ductility and damage suppression in thin ply CFRP angle-ply laminates. Composites A 2015;69:64–71.

[9] Bullegas G, Pinho ST, Pimenta S. Engineering the translaminar fracture behaviour of thin-ply composites. Compos Sci Technol 2016;131:110–22.

[10] Cugnoni J, Frossard G, Amacher R, Botsis J. Translaminar fracture of regular and hybrid thin ply composites: experimental characterization and modelling. In: ECCM18-18th European conference on composite materials, athens. 2018.

[11] Bažant ZP, Planas J. Fracture and size effect in concrete and other quasibrittle materials. Routledge; 2019.

[12] Jalalvand M, Czél G, Wisnom MR. Numerical modelling of the damage modes in UD thin carbon/glass hybrid laminates. Compos Sci Technol 2014;94:39–47.

[13] Jalalvand M, Czél G, Wisnom MR. Damage analysis of pseudo-ductile thin-ply UD hybrid composites–a new analytical method. Composites A 2015;69:83–93.

[14] Sapozhnikov S, Lomov S, Swolfs Y, Carvelli V. Deformation and failure of pseudo-ductile quasi-isotropic all-carbon hybrid FRPS with an open hole under tension. Composites B 2022;237:109870.

[15] Ritchie RO. Mechanisms of fatigue-crack propagation in ductile and brittle solids. Int J Fract 1999;100(1):55–83.

[16] Brocks W, Cornec A, Scheider I. 3.03 - Computational aspects of nonlinear fracture mechanics. In: Milne I, Ritchie R, Karihaloo B, editors. Comprehensive structural integrity. Oxford: Pergamon; 2003, p. 127–209.
[17] Turner C. A re-assessment of ductile tearing resistance. II. Energy dissipation rate and associated R-curves on normalised axes.(retroactive coverage). ECF 8: Fract Behav Design Mater Struct 1990;2:951–68.
[18] Ritchie RO. The conflicts between strength and toughness. Nature Mater 2011;10(11):817–22.
[19] Chen C, Fleck NA, Lu T. The mode I crack growth resistance of metallic foams. J Mech Phys Solids 2001;49(2):231–59.
[20] Li H, Chandra N. Analysis of crack growth and crack-tip plasticity in ductile materials using cohesive zone models. Int J Plast 2003;19(6):849–82.
[21] Cornec A, Scheider I, Schwalbe K-H. On the practical application of the cohesive model. Eng Fract Mech 2003;70(14):1963–87.
[22] Schwalbe K-H, Scheider I, Cornec A. Guidelines for applying cohesive models to the damage behaviour of engineering materials and structures. Springer Science & Business Media; 2012.
[23] Tvergaard V, Hutchinson JW. The relation between crack growth resistance and fracture process parameters in elastic-plastic solids. J Mech Phys Solids 1992;40(6):1377–97.
[24] Kim BW, Nairn JA. Observations of fiber fracture and interfacial debonding phenomena using the fragmentation test in single fiber composites. J Compos Mater 2002;36(15):1825–58.
[25] Dugdale DS. Yielding of steel sheets containing slits. J Mech Phys Solids 1960;8(2):100–4.
[26] Dávila CG, Rose CA, Camanho PP. A procedure for superposing linear cohesive laws to represent multiple damage mechanisms in the fracture of composites. Int J Fract 2009;158(2):211–23.
[27] Turon A, Davila CG, Camanho PP, Costa J. An engineering solution for mesh size effects in the simulation of delamination using cohesive zone models. Eng Fract Mech 2007;74(10):1665–82.
[28] Buckingham E. On physically similar systems; illustrations of the use of dimensional equations. Phys Rev 1914;4(4):345.
[29] Rice JR. A path independent integral and the approximate analysis of strain concentration by notches and cracks. J Appl Mech 1968;35(2):379–86.
[30] McMeeking R. Path dependence of the J-integral and the role of j as a parameter characterizing the near-tip field. In: Flaw growth and fracture. ASTM International; 1977.
[31] ASTM E1820-20b. Standard test method for measurement of fracture toughness. Technical report, West Conshohocken, PA: ASTM International; 2020.
[32] ASTM E399-20a. Standard test method for linear-elastic plane-strain fracture toughness of metallic materials. Technical report, West Conshohocken, PA: ASTM International; 2020.
[33] Pinho ST, Robinson P, Iannucci L. Fracture toughness of the tensile and compressive fibre failure modes in laminated composites. Composit Sci Technol 2006;66(13):2069–79.
[34] Ortega A, Maimí P, González E, Ripoll L. Compact tension specimen for orthotropic materials. Composites A 2014;63:85–93.
[35] Abaqus. 6.14 Documentation. Dassault Syst Simulia Corpor 2014.
[36] Newman J. Stress analysis of the compact specimen including the effects of pin loading. In: Fracture analysis: proceedings of the 1973 national symposium on fracture mechanics, part II. ASTM International; 1974.
[37] Tada H, Paris PC, Irwin GR. The stress analysis of cracks handbook. 3rd ed.. ASME Press; 2000.
[38] Bažant ZP. Size effect. Int J Solids Struct 2000;37(1–2):69–80.
[39] Maimí P, González EV, Gascons N, Ripoll L. Size effect law and critical distance theories to predict the nominal strength of quasibrittle structures. Appl Mech Rev 2013;65(2).
[40] Bažant ZP. Size effect on structural strength: a review. Arch Appl Mech 1999;69(9):703–25.
[41] Bažant ZP. Scaling theory for quasibrittle structural failure. Proc Natl Acad Sci 2004;101(37):13400–7.
[42] Nguyen HT, Dönmez AA, Bažant ZP. Structural strength scaling law for fracture of plastic-hardening metals and testing of fracture properties. Extreme Mech Lett 2021;43:101141.
[43] Morel S. Size effect in quasibrittle fracture: derivation of the energetic size effect law from equivalent LEFM and asymptotic analysis. Int J Fracture 2008;154(1–2):15–26.
[44] Teixeira R, Pinho S, Robinson P. Thickness-dependence of the translaminar fracture toughness: experimental study using thin-ply composites. Composites A 2016;90:33–44.
[45] Furtado C, Arteiro A, Linde P, Wardle B, Camanho P. Is there a ply thickness effect on the mode I intralaminar fracture toughness of composite laminates? Theor Appl Fract Mech 2020;107:102473.
[46] Danzi F, Tavares R, Xavier J, Fanteria D, Camanho P. Effects of hybridization and ply thickness on the strength and toughness of composite laminates. J Compos Mater 2021;55(30):4601–16.
[47] Maimí Vert P, et al. Modelización constitutiva y computacional del daño y la fractura de materiales compuestos. Universitat de Girona; 2007.
[48] Marsden JE, Hughes TJ. Mathematical foundations of elasticity. Courier Corporation; 1994.